Available online at www.sciencedirect.com
SCIENCE DIRECT®
Journal of Solid State Chemistry 177 (2004) 660–669
JOURNAL OF SOLID STATE CHEMISTRY
http://elsevier.com/locate/jssc

Phase stability and non-stoichiometry in *M*-phase solid solutions in the system $LiO_{0.5}$–$NbO_{2.5}$–TiO_2

I.E. Grey,[a,*] P. Bordet,[b] C. Li,[a] and R.S. Roth[c]

[a] *CSIRO Minerals, Box 312, Clayton South, Victoria 3168, Australia*
[b] *CNRS Laboratoire de Cristallographie, BP166, Grenoble 38042, France*
[c] *National Institute of Standards and Technology, Gaithersburg, MD 20899, USA*

Received 4 June 2003; accepted 21 August 2003

Abstract

Phase relations at 1050°C have been determined for *M*-phase solid solutions in the $LiO_{0.5}$–$NbO_{2.5}$–TiO_2 ternary phase system by the quench method. Rietveld analysis has been used to help determine phase boundaries and to study structure composition relations. The *M*-phases have trigonal structures based on intergrowth of corundum-like layers, $[Ti_2O_3]^{2+}$, with slabs of $(N-1)$ layers of $LiNbO_3$-type parallel to (0001). Ideal compositions are defined along the pseudobinary join $LiNbO_3$–$Li_4Ti_5O_{12}$ by the homologous series formula $Li_NNb_{N-4}Ti_5O_{3N}$, $N \geqslant 4$. Homologues with $N \leqslant 10$ lie to the low-lithia side of the $LiNbO_3$–$Li_4Ti_5O_{12}$ join and show extended single-phase solid solution ranges separated by two-phase regions. The composition variations along the solid solutions are controlled by a major substitution mechanism, $Li^+ + 3Nb^{5+} \leftrightarrow 4Ti^{4+}$, coupled with a minor substitution $4Li^+ \leftrightarrow Ti^{4+} + 3\square$, where $\square$ = vacancy. The latter substitution results in increasing deviations from the stoichiometric compositions $A_{2N+1}O_{3N}$ with increasing Ti substitution. The non-stoichiometry can be reduced by re-equilibration at lower temperatures. Expressions have been developed to describe the compositional changes along the solid solutions.
© 2003 Elsevier Inc. All rights reserved.

1. Introduction

As part of a general study on the influences of additives on the kinetics of char reduction of ilmenite we investigated the reactions of lithium-containing additives with iron titanates and titania under reducing conditions [1]. We identified the formation of a new phase with trigonal symmetry and with a powder pattern matching that for the so-called *H*-phase, $Li_2Ti_3O_7$ [2]. Following Tsubone and Shimizu [3] we stabilized the phase with the addition of a small amount of niobia and determined its structure [4] as an intergrowth of corundum-type and lithium niobate (LN)-type layers. Roth and Davis [5] recognized that this phase is a member of a family of phases in the $LiO_{0.5}$–$NbO_{2.5}$–TiO_2 ternary system studied by Villafuerte-Castrejon et al. [6,7], known as the *M*-phases.

The *M*-phase stability region at 1100°C in the system $LiO_{0.5}$–$NbO_{2.5}$–TiO_2 is shown in Fig. 1 (data from Ref. [7]). It has attracted recent interest because of the chemically tunable dielectric properties exhibited by member compositions [8]. Smith and West [9] proposed the general formula $Li_{1+x-y}Nb_{1-x-3y}Ti_{x+4y}O_3$ to describe compositions in the wedge-shaped phase field. In this formula, y represents a site-balanced substitution given by $Li^+ + 3Nb^{5+} \leftrightarrow 4Ti^{4+}$ and x represents the substitution $Nb^{5+} \leftrightarrow Li^+ + Ti^{4+}$, as occurs along the join $LiNbO_3$–Li_2TiO_3 [6]. Smith and West [9] considered that the *M*-phase was a homogeneous solid solution rather than a series of line phases. They noted that X-ray diffraction patterns for the solid solution members displayed trigonal subcells similar to that for $LiNbO_3$ (LN), but with incommensurate superlattice periodicities along the *c*-axis.

Recent structural studies [10] have shown that the *M*-phase region comprises homologous series of phases with trigonal symmetry and with commensurate structures based on ordered intergrowths of corundum-type layers with different width slabs of LN structure, parallel to (0001). The total number of LN + corundum layers per repeating unit, N, has been observed in transmission electron microscopy (TEM) studies [10–12] to vary from ~56 down to 4 as the titania content

*Corresponding author. Fax: +613-9562-8919.
E-mail address: ian.grey@csiro.au (I.E. Grey).

0022-4596/$ - see front matter © 2003 Elsevier Inc. All rights reserved.
doi:10.1016/j.jssc.2003.08.010

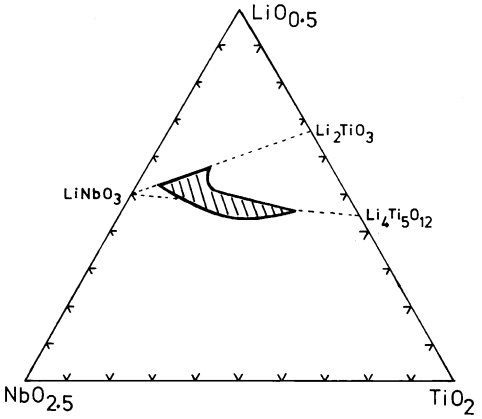

Fig. 1. *M*-phase stability field (shaded) in the ternary system $LiO_{0.5}$–$NbO_{2.5}$–TiO_2 (mol%) at 1100°C, taken from Ref. [7].

increases and the temperature decreases. Phase studies [5] showed that for small values of N ($N<10$) narrow single-phase composition regions were separated by two-phase regions, consistent with normal ternary phase equilibria.

Although the recent studies have clarified the structural principles for describing the homologous series of phases spanning the *M*-phase region, there has been no reported study of the compositional variations within the solid solution fields for individual phases. Such information is useful for understanding the composition and structure dependence of the dielectric properties, needed for designing materials with specific properties. We report here the characterization of the phase stability fields at 1050°C for homologues with $N = 6-10$, including the determination of formulae describing stoichiometry changes within the individual solid solutions, and how the stoichiometry changes with change of temperature.

2. Structural background

A description of the structures of the *M*-phases is presented first, to assist in the subsequent interpretation of the composition-structure variations. The structural principles upon which the *M*-phase structures are based were determined from a combined TEM/powder XRD/neutron diffraction study on a homologue with $N = 5$ by Bordet et al. [4], and confirmed by Farber et al. [10] from a single-crystal structure refinement of a homologue with $N = 10$. The analyses showed that the *M*-phases have trigonal symmetry and have structures based on ordered intergrowth of single layers of corundum-type structure with slabs of $N-1$ layers of LN-type structure, parallel to (0001). Both corundum and LN have *hcp* oxygen lattices and so there is no stacking change of the anion layers at the interfaces. Ti is ordered in the corundum layer, giving $[Ti_2O_3]^{2+}$ charged layers. The remaining Ti and Nb are distributed over the octahedral *M* sites of the LN layers. The central layer(s) of the LN slabs have up to 1 extra Li atom per layer (Li_2MO_3).

The simplest *M*-phase composition is the lithium titanate end member with $N = 4$, having the composition $Li_4Ti_5O_{12}$. The four-layer sequence is $[Ti_2O_3]^{2+}$–$[LiTiO_3]^{-}$–$[Li_2TiO_3]$–$[LiTiO_3]^{-}$–$[Ti_2O_3]^{2+}$. Although the stable form of $Li_4Ti_5O_{12}$ has the spinel structure [13], a four-layer *M*-phase can be prepared in a metastable form at low temperature. Its trigonal unit cell, $a = 5.14$ Å, $c = 9.36$ Å, and four-layer intergrowth character have been confirmed from TEM studies [11]. Successive *M*-phases can be formally derived from the $N = 4$ end member by insertion of layers of composition $LiNbO_3$, giving an homologous series $Li_NNb_{N-4}Ti_5O_{3N} \equiv A_{2N+1}O_{3N}$ with $N \geqslant 4$ and $A = Li/Ti/Nb$. If the compositions of the members of the series are normalized to the same number of oxygen atoms, it is evident that the series involves the site-imbalanced substitution [1] which decreases the [*A*]/[O] ratio with increasing Nb/Ti substitution.

$$5Ti^{4+} \leftrightarrow 4Nb^{5+} \ldots . \quad (1)$$

Representation of the $N = 4$ and 5 structures are given in Fig. 2, showing the key features of the *M*-phase structures. The Ti-centred octahedra in the $[Ti_2O_3]^{2+}$ layers share faces with octahedra in the adjacent layers, as in corundum. For $N = 2n$ homologues the central

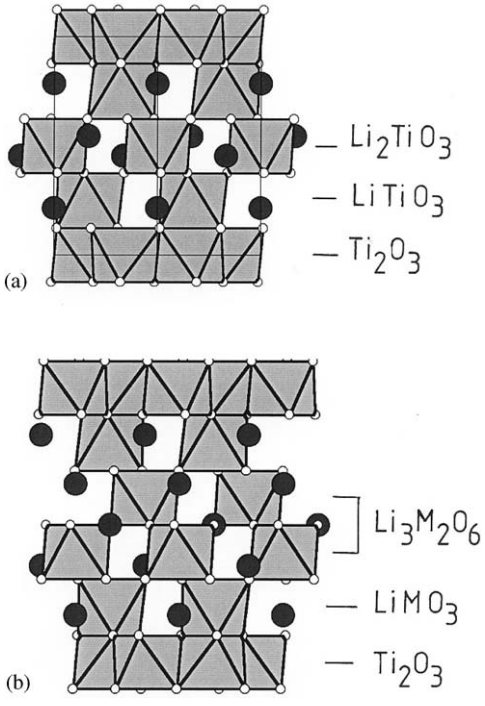

Fig. 2. Polyhedral projections along [110] of the structures of *M*-phase homologues with (a) $N = 4$, $Li_4Ti_5O_{12}$ and (b) $N = 5$, $Li_5NbTi_5O_{15}$. Lithium atoms shown as filled circles. The unit cell outline is shown in (a), the *c*-axis is vertical.

polyhedral layer in the LN slab has composition Li_2MO_3, whereas for homologues with $N = 2n + 1$ the extra Li atom is distributed over two central polyhedral layers, giving a two-layer composition $Li_3M_2O_6$. In this case, the Li atoms lie almost in the plane of the oxygen atoms, as occurs in paraelectric $LiNbO_3$ [14]. Refinements of the structures of the $N = 5$ and 10 homologues [4,10] showed that minor substitution of Ti/Nb into Li sites occurs in the $LiMO_3$ layers, as found for non-stoichiometric LN [15].

An analysis of the metal atom and oxygen stacking sequences in different M-phases [10] shows that a description of all homologues requires four different space groups, $P\bar{3}$, $P\bar{3}c1$, $R\bar{3}$ and $R\bar{3}c$, and that the sequence of space groups follows a periodic pattern, repeating itself at values of N, $N + 6$, $N + 12$, etc. This is illustrated in Fig. 3, where the values of N and Lc, the total number of layers per unit cell, are given for each of the four space groups. Table 1 reports block compositions for the first seven M-phase homologues, $N = 4-10$, together with the number of layers per block (N), the number of blocks per unit cell ($= Lc/N$), and unit cell parameters. The variation in the number of blocks per unit cell between successive M-phases requires different indexing schemes for adjacent homologues. The c-axis dimensions show corresponding large oscillations, even for relatively small values of N, for example c increases from 56 to 125 Å and then decreases to 23 Å as N increases from 8 to 10. This explains why previous researchers had such difficulty in indexing the M-phase powder XRD patterns and why the structures were originally thought to be incommensurate [5,9]. The indexed powder XRD patterns ($2\theta \leqslant 40°$) obtained in the current study for representative samples of the $N = 6-10$ homologues are reported in Table 2. The unit cell parameters obtained from refinement of the full patterns (to $2\theta = 140°$) are given in Table 1.

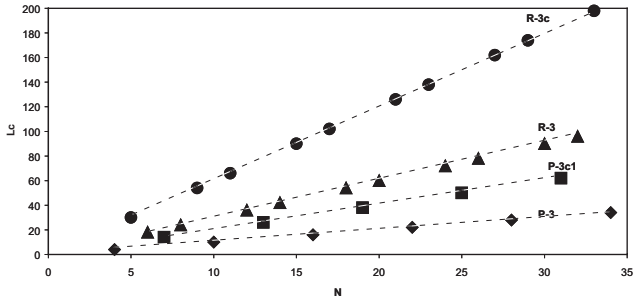

Fig. 3. Variation of N (number of layers per block) and Lc (number of layers per unit cell) for the four space groups that are required to describe the M-phases. The dotted lines connect points corresponding to the same space group.

Table 1
Structure systematics of M-phases with $N = 6$–10

Block composition	N = No. of layers per block	No. of blocks per cell	Space group	Unit cell parameters (Å)	
$Li_4Ti_5O_{12}$	4	1	$P\bar{3}$	5.14	9.36[a]
$Li_5Ti_5NbO_{15}$	5	6	$R\bar{3}c$	5.074	69.940[b]
$Li_6Ti_5Nb_2O_{18}$	6	3	$R\bar{3}$	5.089	41.898[c]
$Li_7Ti_5Nb_3O_{21}$	7	2	$P\bar{3}c1$	5.102	32.557[c]
$Li_8Ti_5Nb_4O_{24}$	8	3	$R\bar{3}$	5.107	55.747[c]
$Li_9Ti_5Nb_5O_{27}$	9	6	$R\bar{3}c$	5.107	125.28[c]
$Li_{10}Ti_5Nb_6O_{30}$	10	1	$P\bar{3}$	5.117	23.198[c]
$LiNbO_3$	1	6	R3c	5.148	13.857[d]

[a] Ref. [11].
[b] Ref. [4].
[c] From refinement of data in Table 2.
[d] Ref. [15].

The preceeding structural description refers to the point compositions, $Li_NNb_{N-4}Ti_5O_{3N}$, lying along the pseudobinary join $LiNbO_3$–$Li_4Ti_5O_{12}$. The experimentally determined M-phase region, shown in Fig. 1 for 1100°C, extends to either side of this join. On the high-$LiO_{0.5}$ side of the join, the stability regions of the individual homologues are extended by increasing replacement of LN layers by Li-rich Li_2MO_3 layers, as described by Farber et al. [10]. On the low-$LiO_{0.5}$ side of the join, the stability fields of the individual homologues are extended mainly by the site-balanced substitution $Li^+ + 3Nb^{5+} \leftrightarrow 4Ti^{4+}$, as will be described below.

3. Experimental

3.1. Phase equilibria studies

Starting materials for the phase equilibria studies were Koch Light TiO_2 and Nb_2O_5 (both 99.99%) and Univar AR grade Li_2CO_3. Weighed mixtures of the starting materials were ground together in anhydrous ethanol then heated for 2 h at 900°C in a muffle furnace in air to decompose the carbonate. The furnace temperature at the sample position was adjusted to the desired value ±5°C using a calibrated reference thermocouple. The samples were then reground in ethanol, dried, and pressed into 12 mm diameter cylindrical pellets. The pellets were placed on top of sacrificial pellets of the same composition in a platinum boat and heated in the muffle furnace at 1050°C for 16 h, then removed from the furnace to cool in air. The pellets were ground in ethanol, repelleted and then reheated for a further 16 h. Powder XRD was used to check for changes in the phase assemblages between successive equilibrations. If necessary, the grinding and reheating procedure was repeated.

X-ray fluorescence (XRF) analyses for Nb and Ti were conducted on selected samples after successive heating periods to check the starting compositions and

Table 2
Indexed low angle powder XRD patterns[a] for representative M-phases with $N = 6-10$ ($CuK\alpha_1$ radiation)

$N=6$			$N=7$			$N=8$			$N=9$			$N=10$		
hkl	2θ	I/I_o	hkl	2θ	I/I_o	hkl	2θ	I/I_o	hkl	2θ	I/I_o	hkl	2θ	I/I_o
0 0 9	19.05	2	0 0 6	16.32	0.5	0 0 12	19.09	1	0 1 2	20.12	1	0 1 0	20.02	0.5
1 0 1	20.24	3	1 0 0	20.08	2	1 0 1	20.12	2	1 0 4	20.27	2	1 0 1	20.38	2
						0 1 2	20.31	1	0 1 8	20.86	1			
0 1 2	20.58	7	1 0 2	20.81	7	1 0 4	21.06	8	1 0 10	21.29	8	1 0 2	21.45	8
1 0 4	21.86	1	0 0 8	21.82	0.5							0 0 6	22.98	0.5
0 1 5	22.78	100	1 0 4	22.88	100	1 0 7	22.98	100	1 0 16	23.08	100	1 0 3	23.11	100
0 0 12	25.49	1				0 0 15	23.94	1						
0 1 8	26.41	29	1 0 6	25.98	32	1 0 10	25.69	36	1 0 22	25.49	39	1 0 4	25.27	38
			0 0 10	27.37	0.5							0 0 7	26.88	0.5
0 1 11	31.01	2	1 0 8	29.82	2	1 0 13	28.98	2	1 0 28	28.36	3	1 0 5	27.81	3
0 0 15	32.02	1	0 0 12	32.99	0.5	0 0 21	33.73	1						
1 0 13	34.45	56	0 1 10	34.18	51	0 1 17	34.01	55	0 1 38	33.89	52	0 1 7	33.74	55
									0 0 48	34.34	0.5	0 0 9	34.77	0.5
1 1 0	35.24	27	1 1 0	35.15	30	1 1 0	35.11	31	1 1 0	35.12	27	1 1 0	35.04	32
1 1 9	40.36	29	1 1 7	40.29	23	1 1 12	40.27	23	1 1 27	40.29	23	1 1 5	40.22	20

[a] Refined unit cell parameters given in Table 1.

to monitor if any lithium loss occurred by volatilization (as evidenced by increased $\sum(TiO_2+Nb_2O_5)$). For the compositions studied, at 1050°C, no detectable losses occurred over combined heating periods of up to 60 h. Selected single-phase samples were re-equilibrated at successively lower temperatures, down to 750°C, to study the movement of phase boundaries and variation of phase stoichiometry with temperature. At the lower temperatures, heating periods of at least 60 h were typically employed.

Rietveld refinements of powder XRD patterns were used to determine unit cell parameters and cation distributions in single-phase products, and to determine the weight percents of co-existing two-phase and three-phase assemblages. Samples for powder XRD were prepared by grinding and back-pressing the powders into an aluminum sample holder. Measurements of diffracted intensities were made using a Philips 1050 goniometer with a PW1710 controller and using a long fine-focus copper tube operated at 40 kV and 40 mA. The diffractometer was configured with a 1° divergent slit, 0.2 mm receiving slit, 1° scatter slit, incident and diffracted beam Soller slits and a diffracted-beam curved graphite monochromator. Step-scan intensity measurements in the 2θ range 10–140° were made at intervals of 0.025°, with a total counting time of 2 h per sample.

Least-squares refinements were conducted using the Rietveld program SR5, a local modification of the code by Hill and Howard [16] and Wiles and Young [17], and the Rietveld component of the JANA program [18]. Starting models for the refinements were constructed using information gained from single-crystal structure determinations for the $N = 5, 7, 8$ and 10 homologues (4,10 and unpublished results).

4. Results and discussion

4.1. Phase equilibria at 1050°C

At the temperature of 1050°C used in this study, M-phases were stable for $N \geqslant 6$. For values of N greater than 10 it became increasingly difficult to distinguish the increasingly narrow two-phase regions separating adjacent M-phases and so the study concentrated on the stability of phases with $6 \leqslant N \leqslant 10$. The experimentally determined single-phase solid solution ranges for the $N = 6-10$ homologues at 1050°C and associated invariant three-phase equilibria with rutile (ss) and Li_2TiO_3 (ss) are shown on the ternary $LiO_{0.5}$–$NbO_{2.5}$–TiO_2 (mol%) diagram in Fig. 4. Dashed lines representing the $LiNbO_3$–$Li_2Ti_4O_9$ join (constant atomic ratio $[Li+Nb+Ti]/[O] = 0.667$) and the $LiNbO_3$–$Li_4Ti_5O_9$ join are shown, together with the compositions of M-phases with different N values along the latter join.

Fig. 4 shows that the M-phases have appreciable solid solubility, the extent of which increases with increasing N from 6 to 10. The single-phase compositions for individual M phases are oriented approximately parallel to the $LiNbO_3$–$Li_2Ti_4O_9$ join, indicating that the site-balanced substitution (2) provides the dominant mechanism for the solid solutions:

$$y\mathrm{Li}^{+} + 3y\mathrm{Nb}^{5+} \leftrightarrow 4y\mathrm{Ti}^{4+} \ldots . \quad (2)$$

However, careful phase equilibria experiments at closely spaced composition intervals shows that the lines defining the solid solutions have slopes that are consistently steeper than the slope expected for the site-balanced substitution. That is, the $[Li+Nb+Ti]/[O]$ atomic ratio decreases with increasing Ti substitution, corresponding to increasing vacancy formation in the

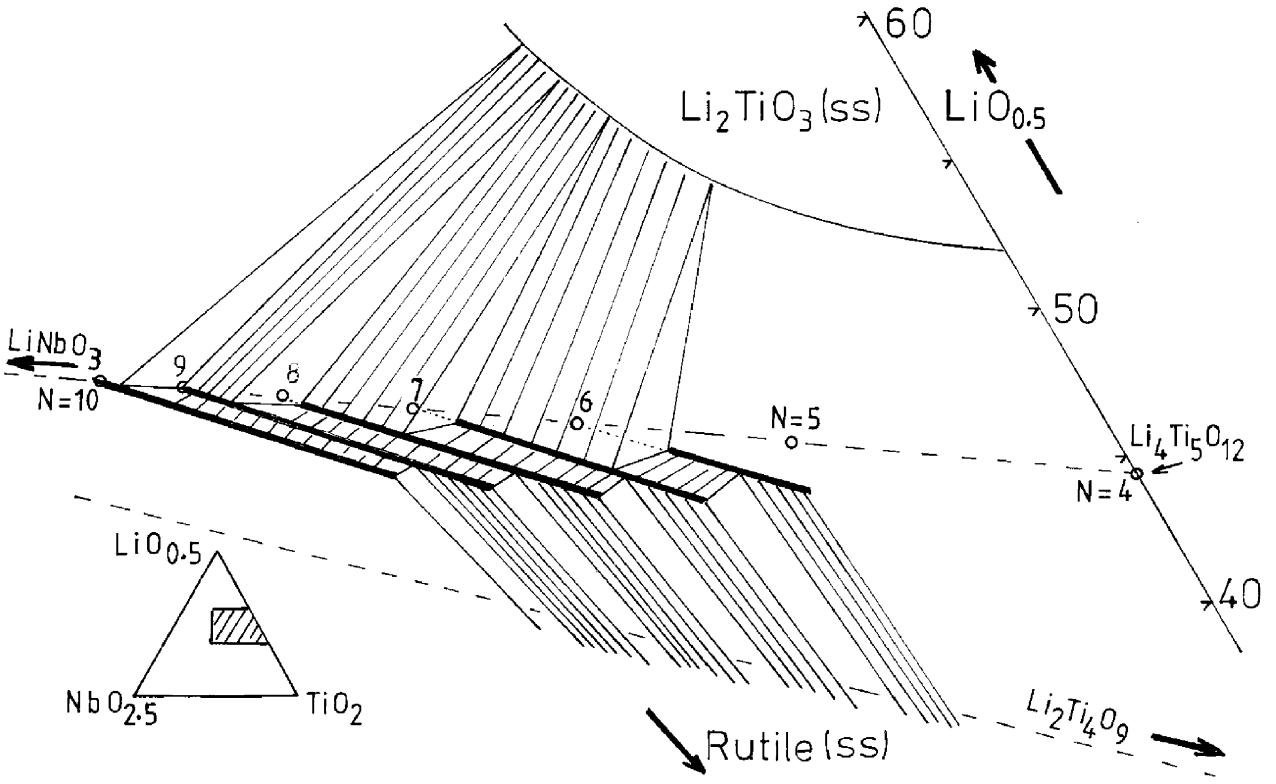

Fig. 4. Phase relations at 1050°C for the *M*-phase solid solutions with $N = 6-10$, plotted on the ternary diagram $LiO_{0.5}$–$NbO_{2.5}$–TiO_2 (mol%).

metal atom lattice. By analogy with non-stoichiometric LN [15], a site-imbalanced substitution of the type (3) needs to be included in the mechanism for the solid solutions.

$$4xLi^{+} \leftrightarrow xTi^{4+} + 3x\square \ldots, \quad (3)$$

where x denotes the extent of substitution and $\square$ = vacant site. Other site-imbalanced substitutions, e.g. $5Li^{+} \leftrightarrow Nb^{5+} + 4\square$ and $Li^{+} + Ti^{4+} \leftrightarrow Nb^{5+} + \square$ are possible, but are less likely because increasing vacancy content is associated with increasing Nb in these cases, rather than increasing Ti as observed experimentally.

The $N = 6-10$ solid solution lines have the same slope, indicating that the ratio of the mechanisms (2) and (3) is constant for the different *M*-phases. Moreover, the most LN-rich compositions for the solid solutions lie on the $Li_4Ti_5O_{12}$–$LiNbO_3$ join at the ideal calculated compositions, $Li_NNb_{N-4}Ti_5O_{3N}$ (for $N = 9$ and 10) or linearly extrapolate to the ideal homologue compositions for $N < 9$. These two experimental observations were used to generate formulae to describe the composition variations in the solid solutions. The general expression for the compositions of single blocks (N layers) is

$$\square_{3Ry}Li_{N-(1+4R)y}Nb_{N-4-3y}Ti_{5+(4+R)y}O_{3N} \ldots, \quad (4)$$

where R is the ratio (3)/(2) and y is extent of (2). The procedure used was to determine the experimental block composition for each single-phase sample from the ratios of [Li]:[Nb]:[Ti] used in the starting mixtures, normalized to $3N$ oxygen atoms. The [Nb] atomic content was then used to calculate y for each sample, from $[Nb] = N - 4 - 3y$. An estimated value of R was used to calculate compositions according to expression (4). The SOLVER routine in Excel was then applied to find the optimum global value of R that minimized the differences between the experimental and calculated atomic contents for all samples ($N = 6-10$). The value thus obtained was $R = 0.1296$. Substituting this value into (4) gave expressions for the solid solution compositions with $N = 6-10$ as a function of y only. These expressions are given in Table 3. The solid solution lines shown in Fig. 4 were calculated with these expressions and were found to give a good fit to the experimental points.

Table 3
Solid solution expressions for $N = 6-10$ homologues, and y limits at 1050°C

N	Solid solution expression	Range of y at 1050°C
6	$\square_{0.389y}Li_{6-1.518y}Nb_{2-3y}Ti_{5+4.130y}O_{18}$	0.10–0.16
7	$\square_{0.389y}Li_{7-1.518y}Nb_{3-3y}Ti_{5+4.130y}O_{21}$	0.05–0.30
8	$\square_{0.389y}Li_{8-1.518y}Nb_{4-3y}Ti_{5+4.130y}O_{24}$	0.01–0.43
9	$\square_{0.389y}Li_{9-1.518y}Nb_{5-3y}Ti_{5+4.130y}O_{27}$	0.00–0.47
10	$\square_{0.389y}Li_{10-1.518y}Nb_{6-3y}Ti_{5+4.130y}O_{30}$	−0.02–0.50

4.2. Rietveld analyses

Rietveld analysis is a powerful tool in phase equilibria studies involving solid solution phases, as in the present study. The Rietveld refinements give accurate unit cell parameter variations as a function of composition variation along the solid solutions. Plots of composition vs. cell parameters can then be used to calculate the tie-lines between co-existing pairs of *M*-phases, and to determine the compositions of *M*-phases in invariant three-phase equilibria regions. An independent check on the results can be made using the weight fractions of the phases, which are also determined in the Rietveld analysis.

Table 4 reports the variation of cell parameters in the $N = 6-10$ solid solutions. This table also gives the starting mole fractions of $LiO_{0.5}$, $NbO_{2.5}$ and TiO_2 for the single-phase samples as well as the block compositions calculated using expression (4) with the y values listed in Table 4. The deviation from the stoichiometric homologue compositions, $A_{2N+1}O_{3N}$, increases (increasing vacancy concentration) with increasing Ti content within each solid solution, due to the increasing contribution of the substitution mechanism (3).

The y value for each phase is plotted against the a cell parameter and against the mean layer separation ($\equiv c/Lc$) in Fig. 5. Within each solid solution (fixed N) both the a cell parameter and the mean layer separation decrease with increasing y, as expected from size considerations as Li and Nb are replaced by Ti due to the dominant substitution mechanism (2). At fixed y values (substitution mechanism (1)), the a cell parameter decreases with decreasing N, as expected due to increasing substitution of Ti for Nb. However, the mean layer separation shows the opposite trend, and *increases* with decreasing N.

The increase in the layer separation along [0001] with decrease in N can be understood in terms of the way the *M*-phase structures accommodate the increased [metal]/[O] ratio associated with the substitution mechanism (1). The extra metal atoms are accommodated by an increased proportion of corundum-type $[Ti_2O_3]^{2+}$ layers and excess-Li layers, Li_2MO_3 or $Li_3M_2O_6$, relative to $LiMO_3$ layers. Interlayer articulation of octahedra in the corundum and excess-Li layers results in face-shared octahedra along the c-axis direction involving Ti–Ti/Nb pairs and Li–Ti/Nb–Li strings. The strong metal–metal

Table 4
Compositional and unit cell data for single-phase products

Run No.	Starting mole fractions			y	Block composition (from (4), $R = 0.1296$)	Cell parameters[a] (Å)	
	$LiO_{0.5}$	$NbO_{2.5}$	TiO_2			a	c
$N = 6$							
LNT44	0.452	0.132	0.416	0.096	$\square_{0.04}Li_{5.85}Nb_{1.71}Ti_{5.40}O_{18}$	5.0982	41.936
LNT43	0.448	0.122	0.430	0.140	$\square_{0.05}Li_{5.79}Nb_{1.58}Ti_{5.58}O_{18}$	5.0946	41.919
LNT42	0.446	0.116	0.438	0.166	$\square_{0.07}Li_{5.75}Nb_{1.50}Ti_{5.68}O_{18}$	5.0933	41.916
LNT8[b]	0.440	0.1025	0.4575	0.225	$\square_{0.09}Li_{5.66}Nb_{1.33}Ti_{5.93}O_{18}$	5.0901	41.907
$N = 7$							
LNT35	0.460	0.190	0.350	0.053	$\square_{0.02}Li_{6.92}Nb_{2.84}Ti_{5.22}O_{21}$	5.1081	32.578
LNT37	0.452	0.170	0.378	0.154	$\square_{0.06}Li_{6.76}Nb_{2.54}Ti_{5.64}O_{21}$	5.1022	32.562
LNT38	0.446	0.156	0.398	0.225	$\square_{0.09}Li_{6.66}Nb_{2.32}Ti_{5.93}O_{21}$	5.0987	32.551
LNT40	0.440	0.140	0.420	0.305	$\square_{0.12}Li_{6.54}Nb_{2.08}Ti_{6.26}O_{21}$	5.0940	32.538
$N = 8$							
LNT22	0.464	0.228	0.308	0.047	$\square_{0.02}Li_{7.93}Nb_{3.86}Ti_{5.19}O_{24}$	5.1144	55.784
LNT7	0.455	0.2035	0.3415	0.186	$\square_{0.07}Li_{7.72}Nb_{3.44}Ti_{5.77}O_{24}$	5.1082	55.761
LNT16	0.442	0.172	0.386	0.366	$\square_{0.14}Li_{7.45}Nb_{2.90}Ti_{6.51}O_{24}$	5.0984	55.715
LNT30	0.438	0.160	0.402	0.434	$\square_{0.17}Li_{7.34}Nb_{2.70}Ti_{6.79}O_{24}$	5.0948	55.697
$N = 9$							
LNT21	0.470	0.264	0.266	0.002	$\square_{0.00}Li_{9.00}Nb_{5.00}Ti_{5.00}O_{27}$	5.1211	125.429
ZLNT1	0.4603	0.2381	0.3016	0.167	$\square_{0.06}Li_{8.75}Nb_{4.50}Ti_{5.69}O_{27}$	5.1134	125.369
LNT45	0.452	0.220	0.328	0.284	$\square_{0.11}Li_{8.57}Nb_{4.15}Ti_{6.17}O_{27}$	5.1081	125.316
LNT29	0.440	0.190	0.370	0.475	$\square_{0.19}Li_{8.28}Nb_{3.57}Ti_{6.96}O_{27}$	5.0994	125.217
$N = 10$							
LNT31	0.476	0.290	0.234	−0.027	$\square_{0.00}Li_{10.03}Nb_{6.08}Ti_{4.89}O_{30}$	5.1263	23.211
LNT9	0.4644	0.2656	0.270	0.151	$\square_{0.06}Li_{9.77}Nb_{5.55}Ti_{5.62}O_{30}$	5.1187	23.204
LNT46	0.456	0.244	0.300	0.303	$\square_{0.12}Li_{9.54}Nb_{5.09}Ti_{6.25}O_{30}$	5.1126	23.193
LNT24	0.446	0.222	0.332	0.460	$\square_{0.18}Li_{9.30}Nb_{4.62}Ti_{6.90}O_{30}$	5.1055	23.181

[a] Rietveld e.s.d.s are typically 0.00004 for a and 0.0003–0.001 for c.
[b] Sample equilibrated at 1000°C.

repulsions associated with these face-shared octahedra are relieved by expansion along c.

The variations of the cell parameters with the compositional parameter y as shown in Fig. 5 were used to determine the compositions of co-existing M-phases in the two-phase regions between adjacent M-phases, and in the three-phase regions terminating the solid solutions, giving the tie lines and phase boundaries shown in Fig. 4. An interesting observation was that the a cell dimension was identical for co-existing pairs of M-phases. This is consistent with high-resolution TEM studies [10,11] that show coherent intergrowth between adjacent homologues parallel to (0001). This suggests that the driving force for the composition/structure adjustments of co-existing M-phases is the minimization of the interfacial energy [11].

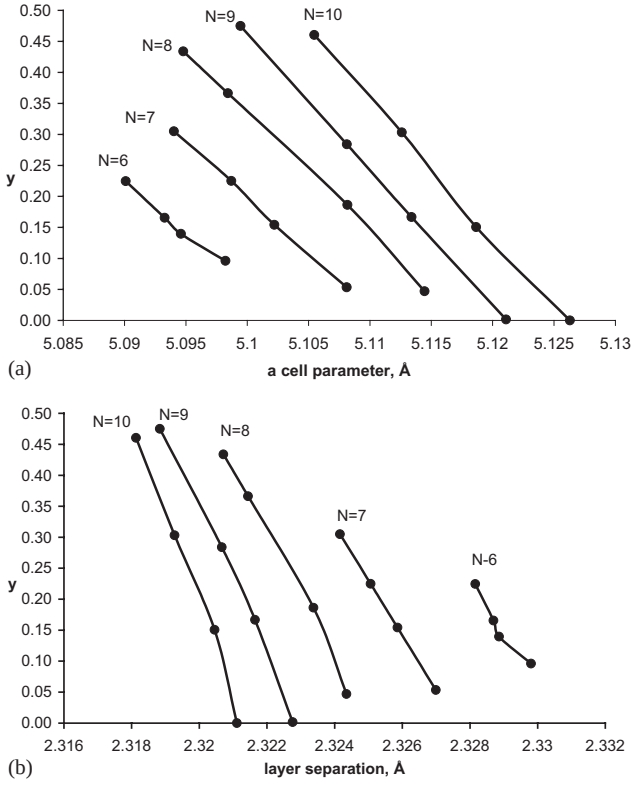

Fig. 5. (a) Plot of y in Table 4 vs. a cell parameter for $N = 6-10$ solid solutions. (b) y vs. the layer separation $= c/\mathrm{Lc}$.

Terminal compositions at the high [Ti] end of the solid solutions co-exist with a solid solution member of the next highest N-value homologue plus rutile solid solution. The cell parameters of rutile in different three-phase mixtures were found to be the same, within the associated standard deviations, $a_r = 4.606(3)$ Å, $c_r = 2.963(3)$. From Garcia et al.'s [19] composition-cell parameter plots for the TiO_2–$LiNb_3O_8$ solid solution, the rutile composition involved in the three-phase equilibria at 1050°C is $Li_{0.025}Nb_{0.075}Ti_{0.90}O_2$.

The M-phase terminal compositions at the high [Li/Nb] end of the solid solutions are in equilibrium with the next lowest N-value homologue plus Li_2TiO_3 solid solution. However, there is no published data for the variation of the cell parameters with composition of Li_2TiO_3 (ss). In this case we used the tie lines between the M-phase region and the Li_2TiO_3 (ss) shown in the phase equilibria study of Villafuerte-Castrejon et al. [7] as a guide to determine Li_2TiO_3 (ss) compositions co-existing with pairs of M-phases in the three-phase equilibria shown in Fig. 4.

4.3. Higher M-phase homologues ($N > 10$)

This study concentrated on phase equilibria for low-N homologues separated by well-defined two-phase regions. As N increases above 10 it becomes more difficult to discern the small XRD peak displacements distinguishing adjacent homologues. Some higher order homologues were prepared and indexed, with N values of or close to 11, 13, 19 and 22. When the compositions were selected to lie below the $LiNbO_3$–$Li_4Ti_5O_{12}$ join, the phases formed solid solutions parallel to the solid solution lines for the lower homologues shown in Fig. 4, indicating that a combination of the substitution mechanisms (2) (dominant) and (3) apply also to the higher N values. Solid solution behavior for M-phases *above* the $LiNbO_3$–$Li_4Ti_5O_{12}$ join can be estimated from the results reported by Borisevich and Davies [8] in their Table 2 and Fig. 4. Above the $LiNbO_3$–$Li_4Ti_5O_{12}$ join the solid solution lines for constant N are directed towards the $LiO_{0.5}$ corner of the ternary diagram. As explained by Farber et al. [10], the excess Li atoms in these compositions are accommodated by increasing the

Table 5
Stoichiometry changes with temperature in selected M-phases

Run No.	Temp. (°C)	Phases (wt%)	M-phase composition	Cell parameters (Å)	
				a	c
LNT3	1050	$N = 7$	$\square_{0.08}Li_{6.72}Nb_{2.46}Ti_{5.74}O_{21}$	5.1022 (1)	32.569 (1)
LNT3A	750	98.3% $N = 7 + 1.7\%$ R(ss)	$\square_{0.00}Li_{6.83}Nb_{2.49}Ti_{5.68}O_{21}$	5.1018 (1)	32.554 (1)
LNT7	1050	$N = 8$	$\square_{0.09}Li_{7.70}Nb_{3.44}Ti_{5.77}O_{24}$	5.1082 (1)	55.761 (2)
LNT7A	750	98.7% $N = 8 + 1.3\%$ R(ss)	$\square_{0.02}Li_{7.80}Nb_{3.48}Ti_{5.70}O_{24}$	5.1084 (1)	55.749 (2)

number of Li_2MO_3 layers relative to $LiMO_3$ layers in the centres of the LN blocks.

4.4. Effect of temperature on the phase boundaries

The stability fields for the lower *M*-phase homologues are sensitive functions of the temperature and niobia content. In previous phase studies at 1100°C, *M*-phases with $N \geqslant 8$ only could be prepared [8]. Decreasing the temperature to 1050°C in this study extended the stability field to $N = 6$ and 7 homologues, albeit with smaller solid solution ranges that for the higher homologues as shown by the ranges in Table 3. At high temperatures the lower homologues are unstable relative to a $Li_2Ti_3O_7$ solid solution phase with the ramsdellite structure [2,7]. The $N = 4$ and 5 homologues can be prepared metastably by quenching the ramsdellite phase and then reheating at low temperatures [3,4,11]. Addition of niobia stabilizes the *M*-phases to higher temperatures. Tsubone and Shimizu [3] found that the addition of 3–5 mol% Nb_2O_5 was necessary to prevent the metastable $N = 5$ homologue decomposing to the stable phase assemblage (below 940°C) of spinel plus rutile.

The present study provides information on the temperature dependence of the stoichiometry of the *M*-phase solid solutions. The value of x, measuring the extent of non-stoichiometry due to mechanism (3), tended towards zero as the equilibration temperature decreased. When single-phase homologues were heated for extended periods at lower temperatures, rutile (ss) progressively exsolved and the vacancy content of the homologue decreased. This is illustrated by the results in Table 5 for $N = 7$ and 8 homologues that were re-equilibrated at 850°C then 750°C for a total time of 120 h. The re-equilibrated products were subjected to Rietveld analyses to determine the cell parameters of the rutile (ss) phase and the weight percents of the rutile and *M*-phases. Using the published [19] cell parameter vs. composition curves for the TiO_2–$LiNb_3O_8$ rutile (ss) together with the phase analyses, the compositions of the re-equilibrated *M*-phases were calculated. These are compared with the compositions of the 1050°C compositions in Table 5. It is seen that for both samples the vacancy content is significantly decreased by the low temperature equilibration. For the $N = 7$ homologue, a vacancy-free $M_{15}O_{21}$ composition was obtained.

Refined lattice parameters for the *M*-phases at 1050°C and at 750° are compared in Table 5. The changes to the *a* cell parameter are negligible while there are small increases in the *c* parameter with increasing temperature, corresponding to increasing non-stoichiometry. Similar small increases in the *c* parameter with increasing non-stoichiometry are reported for LN, $Li_{1-5x}Nb_{1+x}\square_{4x}O_3$ [15], and for the TiO_2-doped LN ternary solid solution [7]. In fact Fig. 2 in Ref. [7] shows the same type of unit cell parameter changes LN that occur for the *M*-phase solid solutions. In particular, LN compositions along the join $LiNbO_3$–$Li_2Ti_4O_9$, corresponding to the site-balanced substitution (2), have both *a* and *c* decreasing with increasing *y* (as in Fig. 5 for the *M*-phases). LN compositions along lines normal to the $LiNbO_3$–$Li_2Ti_4O_9$ join show no change in *a* but have *c* parameters increasing with increasing distance from the join (= increasing metal atom vacancy content relative to M_2O_3), as observed for increasing non-stoichiometry in the *M*-phases. The origins of the non-stoichiometry in the *M*-phases are thus most likely the same as for non-stoichiometric LN.

4.5. Origin of non-stoichiometry in LN and M-phases

The structural origin of the non-stoichiometry in LN has been vigorously debated in the literature for over 30 years. The defect model that is most consistent with diffraction data, physical measurements and energy calculations [20] is that proposed by Lerner et al. [21] and confirmed by Iyi et al. [15] and Zotov et al. [22] using single-crystal XRD and powder XRD and ND refinements. According to this model, Model 1, the structural formula for non-stoichiometric (Nb-rich) lithium niobate is $[Li_{1-5x}Nb_x\square_{4x}][Nb]O_3$. The Nb sublattice is unaffected by stoichiometry changes while the Li sublattice contains both Li vacancies and Nb substituting for Li. A second model with the structural formula $[Li_{1-5x}Nb_{5x}][Nb_{1-4x}\square_{4x}]O_3$ was proposed by Peterson and Carnevale [23] to explain their NMR results (Model 2). The Nb site vacancies required in Model 2 were confirmed in careful single-crystal XRD structure refinements by Abrahams and Marsh [24]. The occupation of Li sites by the excess Nb atoms results in close association of Nb atoms across shared octahedral edges and faces in both models. Smyth [25] considered that this would be energetically unfavorable and proposed a variation of Model 2 with a rearrangement of Nb vacancies and Nb at Li sites to form ilmenite-like linear defects along [0001]. However, as pointed out by Kong et al. [26], Smyth did not take account of the *excess* of Nb at the Li sites, which would still give rise to Nb–Nb pairs. That these are not necessarily detrimental to the stability of LN is indirectly evidenced by the fact that pairs of highly charged cations (Ti^{4+} and Nb^{5+}) occupying face-and edge-shared octahedra are integral to the *M*-phases.

Donnerberg [27] has argued that the energy difference between the above two models (Li vacancies or Nb vacancies) becomes small when the individual defects form large clusters, and so which model applies may be a sensitive function of the crystal growth conditions. A recent TEM study [28] of non-stoichiometric LN confirmed the presence of clustered defects about 10 Å in diameter. The observed TEM images could be

reproduced using a model involving clustering of Nb, with composition Nb_2O_5. However the observed clustering may not reflect the defect structure and instead could be due to exsolution of nanoscale precipitates of niobia-rich phases such as $LiNb_3O_8$ during cooling from the melt, since the non-stoichiometry in LN narrows sharply below about 930°C [29]. Such exsolution in slowly cooled crystals may also be at the origin of different site occupations obtained in single-crystal XRD structure refinements [15,24].

The continuing uncertainty concerning the structural basis for non-stoichiometry in LN prompts caution in considering the more complex situation prevailing in the *M*-phases. However, it is worth noting that the Rietveld refinements consistently showed the presence of up to 10 atom percent substitution of *M* at Li sites in the $LiMO_3$ layers of the *M*-phases, consistent with our previous single-crystal refinement of an $N = 10$ homologue [10]. The level of substitution decreased with decreasing Ti content along each solid solution, and decreased when phases were equilibrated at lower temperatures. That is, the substitution decreased with decreasing non-stoichiometry. The results from Rietveld refinements of LNT3 ($N = 7$) equilibrated at 1050°C and re-equilibrated at 750°C are compared in Table 6 to illustrate this aspect (Li(2) is the site substituted by *M*). The Rietveld analyses showed no evidence for occupation of the vacant octahedral sites in the $LiMO_3$ layers by Ti/Nb.

Table 6
Rietveld refinements[a] for $N = 7$ solid solution member equilibrated at 750°C and 1050°C

		LNT3A equilibrated at 750°C	LNT3 equilibrated at 1050°C
Space group		$P\bar{3}c1$	$P\bar{3}c1$
M(1) 1/3,2/3,*z*	Site occupancy	0.333 Ti	0.333 Ti
	z	−0.0096 (1)	−0.0099(2)
M(2) 1/3,2/3,*z*	Site occupancy	0.245 (4) Ti + 0.088 Nb	0.224 (4) Ti + 0.109 Nb
	z	0.0813 (1)	0.0808 (1)
M(3) 0,0,*z*	Site occupancy	0.195 (4) Ti + 0.138 Nb	0.189 (4) Ti + 0.144 Nb
	z	0.1480 (1)	0.1485 (1)
M(4) 2/3,1/3,*z*	Site occupancy	0.212 (4) Ti + 0.121 Nb	0.196 (3) Ti + 0.137 Nb
	z	0.2164 (1)	0.2168 (1)
Li(1) 0,0,*z*	Site occupancy	0.333 Li	0.333 Li
	z	0.053 (1)	0.053 (1)
Li(2) 2/3,1/3,*z*	Site occupancy	0.333(1) Li + 0.000 Ti	0.311 (3) Li + 0.022 Ti
	z	0.129 (1)	0.130 (1)
Li(3) 1/3,2/3,*z*	Site occupancy	0.333 Li	0.333 Li
	z	0.200 (1)	0.196 (2)
Li(4) 0,0,*z*	Site occupancy	0.167 Li	0.167 Li
	z	0.260 (2)	0.259 (2)
O(1) *x*, *y*, *z*	*x*	0.025 (3)	0.018 (2)
	y	0.393 (2)	0.393 (2)
	z	0.0339 (2)	0.0338 (2)
O(2) *x*, *y*, *z*	*x*	0.292 (4)	0.288 (3)
	y	0.335 (3)	0.321 (2)
	z	0.1075 (2)	0.1076 (2)
O(3) *x*, *y*, *z*	*x*	−0.048 (4)	−0.049 (3)
	y	0.293 (3)	0.289 (2)
	z	0.1796 (3)	0.1795 (2)
O(4) *x*,0,1/4	*x*	0.623 (4)	0.624 (3)
R_p		10.5	8.0
R_{wp}		14.9	11.7
GOF		1.9	3.0
R_{bragg}		3.4	2.7

[a] Compositions and refined cell parameters given in Table 5. Refined B(M), B(Li) and B(O) values are 0.84(2), 0.07(24), 0.60(7) and 0.66(4), 0.08(28) and 0.54(6) Å^2, respectively, for LNT3 and LNT3A.

The high levels of M atom substitution at the Li sites obtained in the refinements of different M-phases are consistent with Model 2 rather than Model 1. However, confirmation of associated M-site vacancies was not possible because of occupation of the M sites by both Ti and Nb. Currently, single-crystal structural analyses of different M-phases are being undertaken in an attempt to further clarify the origin of the non-stoichiometry.

5. Conclusions

The so-called M-phases in the $LiO_{0.5}$–$NbO_{2.5}$–TiO_2 ternary system have trigonal structures based on intergrowth of corundum-like layers, $[Ti_2O_3]^{2+}$, with slabs of $(N-1)$ layers of LN-type parallel to (0001). Ideal compositions are defined along the pseudobinary join $LiNbO_3$–$Li_4Ti_5O_{12}$ by the homologous series formula $Li_NNb_{N-4}Ti_5O_{3N}$, $N \geqslant 4$. Homologues with $N \leqslant 10$ lie to the low-lithia side of the $LiNbO_3$–$Li_4Ti_5O_{12}$ join and show extended single-phase solid solution ranges separated by two-phase regions.

The compositional variations along the solid solutions are controlled by a major site-balanced substitution mechanism, $Li^{+} + 3Nb^{5+} \leftrightarrow 4Ti^{4+}$, coupled with a minor site-imbalanced substitution $4Li^{+} \leftrightarrow Ti^{4+} + 3\square$. The latter substitution results in increasing deviations from the stoichiometric compositions $A_{2N+1}O_{3N}$ with increasing Ti substitution. Expressions have been developed to describe the compositional changes along the solid solutions.

The characterization of the unit cell parameter variations as functions of the composition variations along the solid solutions and normal to them (change of N) has resolved earlier conflicting reported results that were obtained by treating the M-phase region as a homogeneous solid solution rather than as a series of line phases. The definition of the stability fields and stoichiometry ranges of the M-phase homologues has potential applications in tailor-making phases with specific dielectric properties.

References

[1] I.E. Grey, L.M.D. Cranswick, C. Li, L.A. Bursill, J.L. Peng, J. Solid State Chem. 138 (1998) 74–86.

[2] J.C. Mikkelsen Jr., J. Am. Ceram. Soc. 63 (1980) 331–335.

[3] D. Tsubone, T. Shimizu, J. Ceram. Soc. Jpn. Int. Ed. 101 (1993) 637–641.

[4] P. Bordet, C. Bougerol-Chaillout, I.E. Grey, J.L. Hodeau, O. Isnard, J. Solid State Chem. 152 (2000) 546–553.

[5] R.S. Roth, K.L. Davis, in: ACerS Ann. Meet, 89th. The American Ceramic Society, Westerville, OH, 1987, p. 88;
R.S. Roth, K.L. Davis, in: R.S. Roth (Ed.), Phase Equilibria Diagrams, Vol. XI, The American Ceramic Society, Westerville, OH, 1995, pp. 231–232.

[6] M.E. Villafuerte-Castrejon, J.A. Garcia, E. Cisneros, R. Valenzuela, A.R. West, Br. Ceram. Trans. J. 83 (1984) 143–145.

[7] M.E. Villafuerte-Castrejon, A. Aragon-Pina, R. Valenzuela, A.R. West, J. Solid State Chem. 71 (1987) 103–108.

[8] A.Y. Borisevich, P.K. Davies, J. Am. Ceram. Soc. 85 (2002) 573–578.

[9] R.I. Smith, A.R. West, Mater. Res. Bull. 27 (1992) 277–285.

[10] L. Farber, I. Levin, A. Borisevich, I.E. Grey, R.S. Roth, P.K. Davies, J. Solid State Chem. 166 (2002) 81–90.

[11] J. Zou, F.H. Li, D.Y. Yang, Y.D. Jiang, K.H. Kuo, Philos. Mag. B 57 (1988) 103–110.

[12] H. Hayasi, H. Nakano, K. Suzumura, K. Urabe, A.R. West, in: C. Galassi (Ed.), Fourth Euro Ceramics: Basic Science—Developments in Processing of Advanced Ceramics—Part II, Vol. 2, Gruppo Editoriale Faenza Editrice, Italy, 1995, pp. 391–398.

[13] G.H. Jonker, Trab. Reun. Int, React. Solidos, 3rd, 1956, 1 (1957) pp. 413–421.

[14] H. Lehnert, H. Boysen, F. Frey, A. Hewat, P. Radaelli, Z. Kristallogr. 212 (1997) 712–719.

[15] N. Iyi, K. Kitamura, F. Izumi, J.K. Yamamoto, T. Hayashi, H. Asano, S. Kimura, J. Solid State Chem. 101 (1992) 340–352.

[16] R.J. Hill, C.J. Howard, J. Appl. Crystallogr. 18 (1985) 173–180.

[17] D.B. Wiles, R.A. Young, J. Appl. Crystallogr. 14 (1981) 149–151.

[18] V. Petricek, M. Dusek, The Crystallographic Computing System JANA2000, Institute of Physics, Praha, Czech Republic, 2000.

[19] J.A. Garcia, M.E. Villafuerte-Castrejon, J. Andrade, R. Valenzuela, A.R. West, Mater. Res. Bull. 19 (1984) 649–654.

[20] H.J. Donnerberg, S.M. Tomlinson, C.R.A. Catlow, O.F. Schirmer, Phys. Rev. B 40 (1989) 11909–11916.

[21] P. Lerner, C. Legras, J.P. Dumas, J. Crystal Growth 3,4 (1968) 231–235.

[22] N. Zotov, H. Boysen, F. Frey, T. Metzger, E. Born, J. Phys. Chem. Solids 55 (1994) 142–152.

[23] G.E. Peterson, A. Carnevale, J. Chem. Phys. 56 (1972) 4848.

[24] S.C. Abrahams, P. Marsh, Acta Crystallogr. Sect. B 42 (1986) 61–68.

[25] D.M. Smyth, in: Proceedings of the Sixth IEEE International Symposium on the Applications of Ferroelectricity, Bethlehem, PA, June 1986, pp. 115–117.

[26] Y. Kong, J. Xu, X. Chen, C. Zhang, W. Zhang, G. Zhang, J. Appl. Phys. 87 (2000) 4410–4414.

[27] H. Donnerberg, J. Solid State Chem. 123 (1996) 208–214.

[28] C. Leroux, G. Nihoul, G. Malovichko, V. Grachev, C. Boulesteix, J. Phys. Chem. Solids 59 (1998) 311–319.

[29] L.O. Svaasand, M. Eriksrud, A.P. Grande, F. Mo, J. Crystal Growth 18 (1973) 179–184.